

Low-Order Modeling of Flapping Flight with Highly Articulated, Cambered, Heavy Wings

Xiaozhou Fan* and Kenneth Breuer†
Brown University, Providence, Rhode Island 02912

<https://doi.org/10.2514/1.J060661>

A three-dimensional low-order modeling technique is described for modeling both wing inertial and aerodynamic forces of animals and robots flapping heavy and morphing wings. The model is applied to prescribed kinematics from a previously measured flight of a lesser-nosed, dog-faced fruit bat (*Cynopterus brachyotis*) in straight and climbing flight. Quasi-steady blade element momentum theory is used to model the aerodynamic forces of the highly articulated wing, and a Lagrangian equation of motion is adopted to describe the overall wing-body dynamics that includes the wing inertia. These two distinct and independent models yield a good prediction of the thrust/drag balance, and are in excellent agreement of lift production. Unique to this approach, the quantitative effect of wing camber was examined within the framework, which contributes as much as 27% of the cycle-averaged lift, with a smaller price (10%) paid to drag.

Nomenclature

C_d	=	drag coefficient used for each blade element
C_l	=	lift coefficient used for each blade element
C_{rot}	=	rotational lift coefficient used for each blade element
c	=	chord length
f	=	flapping frequency
i	=	index for the wing segment
\hat{i}	=	i th blade element local streamwise direction
\hat{j}	=	i th blade element local spanwise direction
\hat{k}	=	i th blade element local vertical direction
U	=	magnitude of body velocity
X	=	streamwise direction in global coordinate \mathbf{G}
Y	=	sideslip direction in global coordinate \mathbf{G}
Z	=	vertical direction in global coordinate \mathbf{G}
x	=	thrust direction in body-fixed coordinate \mathbf{B}
y	=	lateral direction in body-fixed coordinate \mathbf{B}
z	=	lift direction in body-fixed coordinate \mathbf{B}
α	=	effective angle of attack
α_0	=	zero lift angle of attack
ρ	=	air density

I. Introduction

RESEARCH in flapping wing flight has advanced dramatically over the last two decades, with growing interest in both understanding biological flight and building bio-inspired flapping wing robots [1,2]. Studies on animals such as the bumblebee (*Bombus impatiens*) [3], the desert locust (*Schistocerca gregaria*) [4], the hawkmoth (*Manduca*) [5], the painted lady butterfly (*Vanessa cardui*) [6], and the fruit fly (*Drosophila*) [7] have revealed the important effects of wing kinematics to the formation and breakdown of the leading-edge vortex (LEV). Studies with larger animals, such as the thrush nightingale (*Luscinia luscinia* L) [8] and rock pigeon [9–11], highlight additional features that birds exhibit with their more flexible and articulated wing structure. For example, during upstroke, birds actively fold their wings to reduce the wetted surface area and in

this way minimize negative lift generated [10,12,13]. Through experiment methods such as Particle Image Velocimetry (PIV) measurements [14–16], it is revealed that bats accentuate these additional degrees of flight complexity with their highly articulated membrane wings, which contribute to bats' extreme flight maneuverability and agility.

Quantitative modeling and simulation of flapping flight and, more recently, robotic flight have also been explored in the past decades. Although large-scale unsteady computational fluid dynamics (CFD) simulations have revealed many important complex flow features associated with flapping flight [13,17–19], low-order modeling [7,20–22] has certain advantages over CFD as being much cheaper in terms of both computational resources and time needed, while maintaining first-order physics.

While it is true that low-order modeling often assumes a quasi-steady assumption and does not have an explicit representation on the unsteady behavior of LEV, a recent effort blended classical unsteady aerodynamic model with quasi-steady prediction, and addressed the contribution of a stabilized LEV, which is based on an extension to Duhamel's principle to nonconventional lift curves [23].

With respect to modeling aerodynamics, blade element momentum theory (BEMT) [24,25] has been developed into an invaluable tool for estimating the aerodynamic forces associated with animal wing motions [26,27]. However, quite a few studies [20,21,25,28,29] would first define a stroke plane, based on which the flapping angle, stroke plane deviation, and wing rotation are then introduced. Other studies would bypass the stroke plane by representing the kinematics of the whole wing temporally using a harmonic function [10,11,30] and a linear velocity variation along the span by a representative anatomy marker extracted from measurement (e.g., the wrist location in [26] or the wing tip in [29]).

These approaches are arguably suitable for an insect wing, where the deformation of the wing geometry is relatively small and a characteristic marker to define the stroke plane is clear. However, for a highly articulated wing, such as that processed by a bird or a bat, the kinematic and geometric variation along span is much more pronounced and highly nonlinear, and this might yield an ill-defined stroke plane [29]. Because the kinematics of each blade element is of paramount importance as the ensuing aerodynamics are contingent on it, oversimplification might incorrectly quantify critical features such as the effective angle of attack or the segment velocity. Moreover, although CFD studies have identified the importance of wing camber on aerodynamics [4–6,29,31,32], there has yet to be a low-order study to flapping wing flight that incorporates camber into the aerodynamic model.

The importance of inertial effects of wing motion on overall flight dynamics has also been shown to be critical [33], particularly in the case of bats who have relatively large fractions of their body mass distributed in their wings [12,34]. For these animals, accelerating

Presented as Paper 2021-0344 at the 2021 AIAA SciTech Forum, Virtual Event, January 11–21, 2021; received 24 February 2021; revision received 28 June 2021; accepted for publication 23 August 2021; published online 28 September 2021. Copyright © 2021 by the American Institute of Aeronautics and Astronautics, Inc. All rights reserved. All requests for copying and permission to reprint should be submitted to CCC at www.copyright.com; employ the eISSN 1533-385X to initiate your request. See also AIAA Rights and Permissions www.aiaa.org/randp.

*Graduate Research Assistant, Center of Fluid Mechanics, School of Engineering (Corresponding Author).

†Professor, Center of Fluid Mechanics, School of Engineering. Associate Fellow AIAA.

heavy wings requires additional forces and torques, and any low-order model that hopes to address flight power requirements must account for wing mass that, due to complex wing articulation, can redistribute and re-orient during the wingbeat cycle.

Finally, the body acceleration (“recoil”) due to heavy wing motion can be substantial [22,35–37]. Specifically, Orlowski and Girard [38] coupled the equation of motion with quasi-steady aerodynamic models, and simulated body response under wings of different mass. Taha et al. [33] studied the stability of a hawkmoth scale system near hovering, and pointed out that the widely used cycle-averaged approach failed to approximate instantaneous force prediction for larger mass ratios. For a hawkmoth-scale system, Biswal et al. [39] designed a Linear Quadratic Regulator (LQR) controller based on the cycle-averaged body dynamics, neglecting the motion and the mass of the wings (which only contribute 6% to the total body mass). This controller was then successfully applied to a full wing-body simulation. However, birds and bats typically fly with much heavier wings (up to 25% in [12,26]), but the importance of the wing mass has been largely omitted in discussion of bat- or bird-scale animal flight [26,29].

The present paper attempts to address these needs and demonstrates progress toward the development of a fully consistent three-dimensional (3D), low-order model. This model uses prescribed kinematics to simulate aerodynamic and inertial forces associated with flapping flight animals, and robotic flight vehicles, which are characterized by highly articulated and flexible thin wings. Here, we introduce a new technique to directly discretize the complicated, deforming bat wing into a set of wing segments, where each segment has six degrees of freedom, includes camber, and is capable of representing complex local kinematics with high fidelity. The model employs BEMT, including the wake effect (i.e., the induced velocity), to estimate aerodynamic forces. Although a quasi-steady basis is assumed, the empirical lift and drag coefficients used in BEMT do reflect some delayed stall characteristics and the lift increment due to the LEV [7,40]. Though the unsteady behavior of the LEV (shedding and forming) is beyond the scope of this paper [23], the rotational lift and the wake models are calculated to address some aspects the unsteadiness in the flow [41]. In addition, the time-varying distribution of wing mass is also accounted for in the Lagrangian equation of motion (LEoM), allowing us to simulate the body recoil motion in reaction to wing motion. In this paper we focus on the description and validation of the method, demonstrating it using a detailed set of kinematics recorded from a bat flying in a wind tunnel [42]. We emphasize that the approach uses prescribed wing and body kinematics. In this sense, it is similar to other studies of flapping flight that use either experimental or theoretical wing kinematics [13,18,21–23,38,43]—none of which treat the fluid–structure interaction and deformation of the wing and body due to the balance between aerodynamic and elastic forces. The fluid–structure interaction problem is, of course, a critical issue to address, but it is beyond the scope of the current paper.

The paper is organized as follows: In the next section, we describe in detail our approach for breaking the wing into segments, defining the wing camber, the resultant aerodynamic/inertial forces, and our approach for combining these into a LEoM. Lastly, we discuss the Monte Carlo simulations to assess the sensitivity to experimental and modeling uncertainty. In Sec. III we apply the method to experimental data of a bat flying in a wind tunnel, and compare our predicted results for the trajectory with those measured by Riskin et al. [42]. We conclude, in Sec. IV, with a summary of the strengths and weakness of this approach, and recommendations for future efforts.

II. Methods

A. Experimental Data

The kinematics analyzed in this paper are derived from previously recorded flight of the lesser-nosed, dog-faced fruit bat, *Cynopterus brachyotis*, in a wind tunnel [12,42]. These medium-sized bats weigh about 34 g and typically have a maximum wing area of ~ 0.25 m², a wingspan of approximately 36 cm, and an average chord $c = 6$ cm, which yields an aspect ratio 6. The experimentally recorded flight speeds range from 3.25 to 7.43 m/s. However, as mentioned before, in this paper, we focus on a single flight in which the net airspeed of the bat was $U = 4.75 \pm 0.20$ m/s. The chord Reynolds number $Re = Uc/\nu$ is thus calculated to be 15,700, and the Strouhal number $St = fh_a/U = 0.4$, where ν is the kinematic viscosity of air, the flapping frequency $f = 9.57$ Hz, and the wingbeat amplitude $h_a = 0.2$ m.

As seen in Fig. 1a, the wing and body kinematics were determined from 3D stereo tracking of markers placed on around 50 anatomical locations on the animal’s trunk and left wing, and recorded at 1000 frames per second; the time duration of this flight was around 0.4 s. The flight was nearly left–right symmetric, and so, by assuming that the right wing motion is the mirror image of the left wing, a complete model of the body kinematics could be generated.

The tracked locations of wing markers were interpolated and filtered using imputation [44] to address the occasional occlusion and digitizing noise present in the dataset. Trimmed score regression (TSR) not only infers the position of occluded markers, but also filters noise stemming from stereo triangulation. This technique takes consideration of the temporal evolution of a marker, as well as the spatial information, such as the relative locus of neighborhood markers. Here, two representative marker trajectories (body and wing tip) are presented in Fig. 1b. Note that wing tip marker (gold in Fig. 1b) has more occlusion than the body marker (orange). The raw data (black) is first detrended and normalized, which helps TSR equally weight markers with either large (e.g., membrane wing markers) or small (e.g., body markers) oscillatory motion.

A global inertial coordinate system G was defined (Fig. 2a). The X axis points in the streamwise direction of the wind tunnel, and

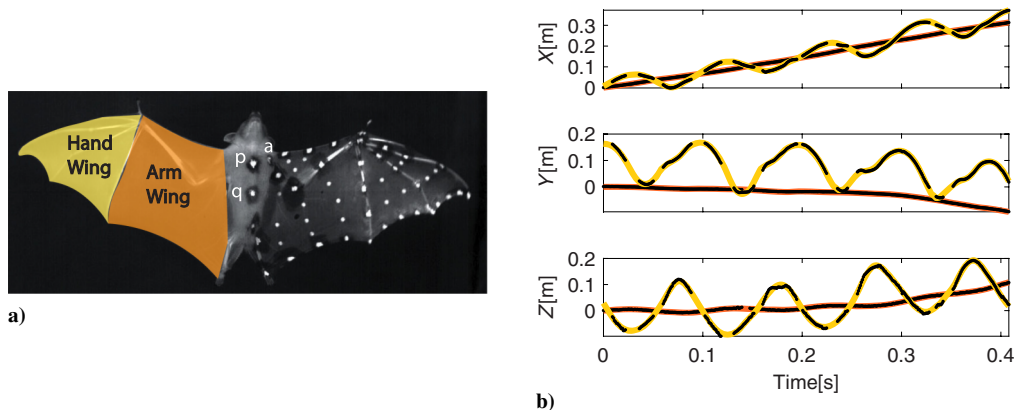


Fig. 1 Data conditioning. a) Marker distribution (ventral side). b) The imputed X , Y , and Z coordinates from sternum (orange), wing tip (gold) and the raw data (black dots) are presented.

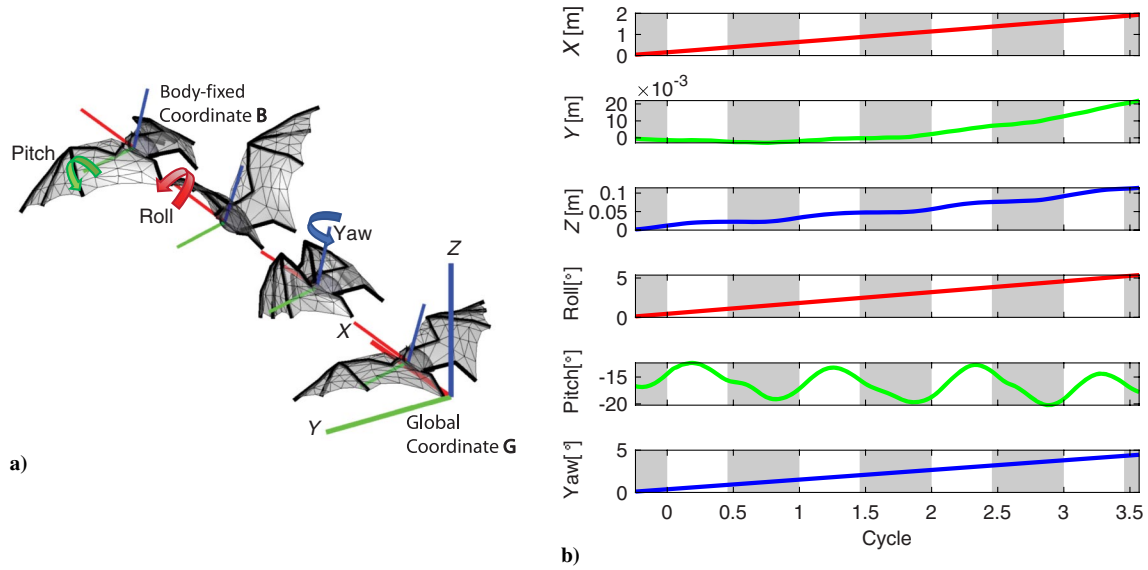


Fig. 2 Definition of coordinates. a) Snapshots of the body-fixed coordinate, B . b) The 6 DoFs of body-fixed coordinate in global coordinate, G . Gray shades indicate downstroke.

the Z axis is vertical, pointing upward toward the ceiling of the tunnel. The Y axis could then be determined by the right-hand rule. As seen in Fig. 1a, the sternum marker (labeled “p”) was chosen to be the origin of the body-fixed coordinate B . The lumbar-sternum vector (in Fig. 1a, “q-p”) is the heading (x axis) of B , and the y axis of B is the surface normal of the triangle “a-p-q,” where “a” is the left shoulder marker. The z axis then follows the right-hand rule. As seen in Fig. 2a, the origin of the body-fixed coordinate B travels with the bat in three translational directions and undergoes three consecutive Euler rotations as yaw (ψ_b), roll (ϕ_b), and pitch (θ_b).

The X , Y , and Z coordinates of the sternum marker in G are given in Fig. 2b, along with the three Euler angles associated with the orientation of the body. Time is nondimensionalized by the duration of the average wingbeat period calculated over the duration of the measured flight; there was three complete flapping cycles. The gray-shaded area represents the downstroke identified by the peaks and troughs of the z component of the shoulder marker in B . The duration of downstroke lasts slightly longer than that of the upstroke. This flight is predominantly straight with a gentle climb, as evidently supported by the X and Z in Fig. 2b. There is minimum body roll and

yaw (both are ~ 5 deg over the course of flight). The body pitch fluctuates around -10 to -20 deg, and the nose-up motion happens mainly in downstroke. In the global coordinate G , the bat travels forward (X direction) for about 2 m, gaining height (Z direction) of about 20 cm. The sideslip (Y direction) is rather small (~ 3 cm).

B. Wing Kinematics and Camber

To model both inertial and aerodynamic measurements, the wing is segmented into a series of discrete blade elements [24]. The wing was divided into $N = 10$ segments, as the number of segments is shown to have only marginal effect on the aerodynamic calculations for $N > 10$. Concretely in Fig. 3a, the span line, defined as a curve (purple “QC”) that connects the quarter-chord of all the segments, is derived from the leading and trailing edge lines (“LE” and “TE,” respectively). It determines the three translational degrees of freedom (DoF) in $B(x_i, y_i, z_i)$ for the i th segment. To define the rotational DoF, the bearing of each segment is constructed as a line from the TE to LE; then the span direction of each segment is defined as the vector direction tangent to the span line (“QC”). The third axis (segment surface normal) then follows the right-hand rule. The three Euler

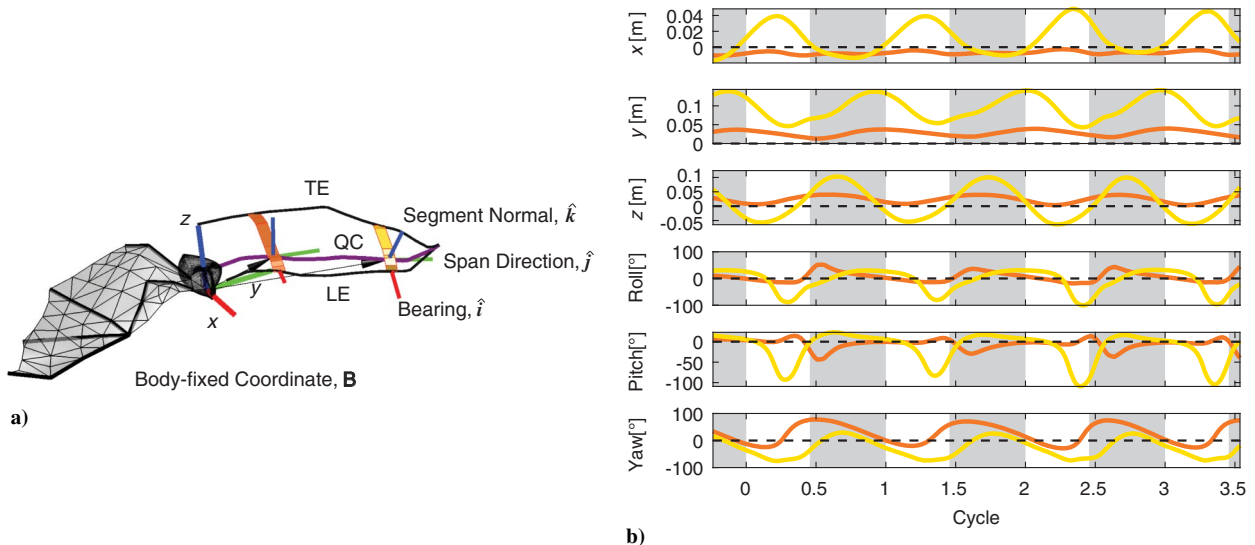


Fig. 3 Segment kinematics in body-fixed coordinate B . a) Two segments are selected to represent arm and hand wing kinematics, each having its own local axes. b) Quantitative description of 6 DoF evolution for hand (1/4 span, in orange) and arm (3/4 span, in gold) wing. The gray shades indicate downstroke.

angles for the i th segment (yaw, roll, and pitch) can thus be calculated. In other words, the i th blade element is uniquely defined by the quarter-chord location relative to the origin of the body-fixed coordinate \mathbf{B} , (x_i, y_i, z_i) , as well as the element orientation, defined by Euler angles, ϕ_i, ψ_i, θ_i , again, with reference to the body-fixed coordinate system \mathbf{B} . Two wing segments, located at the 1/4- and 3/4-span respectively, are selected to be studied in detail. In general, as shown in Fig. 3b, the segment in the distal part of the wing (the “hand wing”) exhibits more pronounced oscillatory motion than the proximal segment (the “arm wing”), as the excursions of the hand wing segment (gold) are larger than those of the arm wing segment (orange) in all directions. The relative motion between the two segments can be readily extended to understand the motion of hand and arm wing as well, where the difference in y reflects the wing folding and that the difference in pitching angles is due to the wing twist along the span. Interestingly, both the hand and arm wing orient similarly during downstroke, but differ greatly during upstroke, when the hand wing starts to thrust forward (yaws as large as -100°) and pitches up (also around -100°). This combined rotation results in the hand wing being almost perpendicular to the floor, with the left and right palms facing each other. This articulation greatly reduces the wetted surface area seen by the incoming flow and ultimately translates to a reduction in negative lift during the upstroke, which will be discussed in more detail in the results section on the aerodynamics of hand and arm wing. Note that this novel discretization process does not need the definition of a stroke plane, and that the detailed local kinematics could thus be preserved.

C. Camber

Previous BEMT models wings as rigid airfoils with a prescribed drag polar [7,10,22,45,46]. Here, however, the thin wings can exhibit substantial deformation during the wing stroke, and so we model the geometry of each blade element as a two-dimensional thin airfoil with a variable camber. The angle of attack and camber are calculated by fitting a Fourier series to the measured data and using thin airfoil theory to associate the Fourier coefficients with the camber of the airfoil [47]. The camber ultimately translates to a zero-lift angle of attack α_0 . Specifically, at each time t_k , a Delaunay triangulation is performed on the wing marker distribution. This mesh structure (see right wing in Fig. 3a) pierces the vertical plane of each segment, forming a set of

points that describe the wing surface in the segment plane (Fig. 4a, black dots). These points are fitted, in the least-squared error sense, with the first two modes of a Fourier sine series (Fig. 4b). The coefficients of these modes are directly related to the zero lift angle of attack α_0 [47]. The first mode (blue) captures the angle of incidence in the local segment axes, and the second mode (green) relates the camber, the combination of which yield the cambered segment (red).

Both the hand and arm wing start with little or no camber at the beginning of downstroke, but become more bulged toward the end of downstroke due to the aerodynamic loading, reaching about 10% of the chord (Fig. 5a). Interestingly for the arm wing, even during upstroke, the camber of the arm wing continues to grow due to the combined motion of legs and elbows, and peaks ($\sim 15\%$ of the chord) at late upstroke, before it drops precipitously as the legs swing back and upward to align with the body. For the hand wing, the camber increases as the digits curl inward at the onset of the upstroke and decreases sharply toward the end of upstroke, when the fingers start to spread outward and prepare for the next downstroke.

D. Aerodynamic Forces

In this paper, blade element theory [7,10,11,21,24,46] is used to model the aerodynamic forces for both the quasi-steady translational component as well as the unsteady rotational lift [46]. In contrast to the lift characteristics of traditional wings [48], the shape of the lift curve used here does incorporate delayed stall characteristics [40]. Finally, a wake model is used to incorporate the finite-wing effect, generating an induced velocity field.

Specifically, for the i th blade element, the total force $\Delta \mathbf{F}_i$ has two components:

$$\Delta \mathbf{F}_i = \Delta \mathbf{F}_{\text{trans},i} + \Delta \mathbf{F}_{\text{rot},i} \quad (1)$$

where $\Delta \mathbf{F}_{\text{trans},i}$ is the aerodynamic force due to the translational motion of the wing, whereas $\Delta \mathbf{F}_{\text{rot},i}$ corresponds to the force generated by the wing rotation [46,49]. Furthermore, we can separate the translational force in terms of lift and drag:

$$\Delta \mathbf{F}_{\text{trans},i} = \Delta \mathbf{L}_i + \Delta \mathbf{D}_i \quad (2)$$

where the segment-wise lift $\Delta \mathbf{L}_i$ and drag $\Delta \mathbf{D}_i$ are then given as

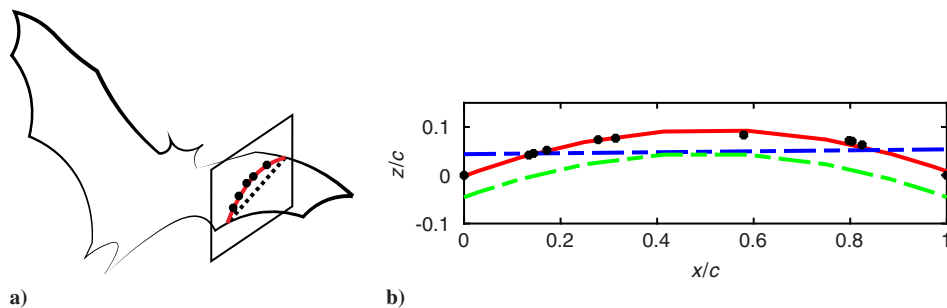


Fig. 4 Camber of the membrane wing due to aerodynamic and wing inertial forces. a) The vertical segment plane intersects the surface mesh generated by the experimental markers. b) The first mode (blue), second mode (green), and the sum of the two modes (red) from the Fourier series are fitted to the raw data (black dots).

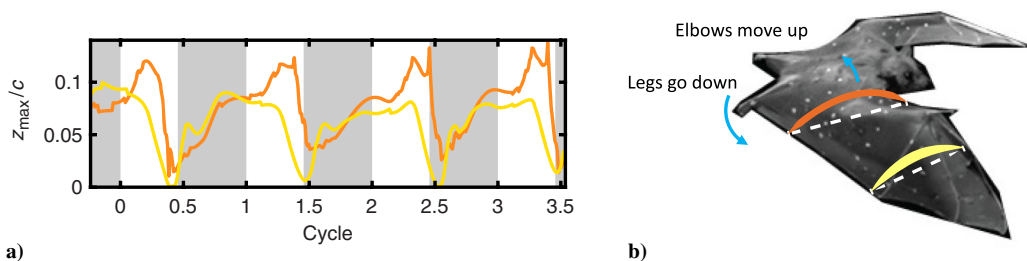


Fig. 5 The time evolution of camber. a) The nondimensionalized camber for arm wing (orange) and the hand wing (gold). The gray shades indicate downstroke. b) For the arm wing, the legs control the ventral-dorsal movement of the trailing edge, whereas the elbow moves out of phase with the leg to control the camber.

$$\Delta \mathbf{L}_i = 1/2 \rho c_i \Delta r_i C_l |\mathbf{U}_i| (\mathbf{U}_i \times \hat{\mathbf{j}}) \quad (3)$$

$$\Delta \mathbf{D}_i = -1/2 \rho c_i \Delta r_i C_d |\mathbf{U}_i| \mathbf{U}_i \quad (4)$$

where ρ , c_i , Δr_i , and \mathbf{U}_i are the air density, chord length, width, and velocity vector of the i th segment in the global coordinate system \mathbf{G} . Due to the highly articulated nature of the bat wing, both c_i and Δr_i vary with time as the result of the wing extending and retracting. The unit vector $\hat{\mathbf{j}}$ is the segment spanwise direction (Fig. 2a). The lift and drag forces on each segment are located at the quarter-chord position (theoretically the aerodynamic center [47]) of the segment. Finally, the aerodynamic coefficients used in the lift (C_l) and drag (C_d) are taken as

$$C_l = A \sin(2(\alpha - \alpha_0)) \quad (5)$$

$$C_d = B - C \cos(2(\alpha - \alpha_0)) \quad (6)$$

where A , B , and C are empirical constants derived from experiments [10,40], and α and α_0 are the effective and zero-lift angles of attack for this segment, respectively. Note that the experimentally obtained coefficients A , B , and C here already contained some delayed stall characteristics at large angles of attack [7,40].

The rotational component of the aerodynamic force, $\Delta \mathbf{F}_{\text{rot},i}$, is given by [21,46]

$$\Delta \mathbf{F}_{\text{rot},i} = C_{\text{rot}} \rho c_i^2 \dot{\theta}_i |\mathbf{U}_i| \Delta r_i \hat{\mathbf{k}} \quad (7)$$

where the rotational force coefficient C_{rot} is given by $C_{\text{rot}} = \pi(0.75 - x/c)$, and $x/c = 0$ and 1 refer to the leading and trailing edge, respectively [49]. For simplicity, we assumed that the pitching axis is the quarter-chord location; $\dot{\theta}_i$ is the angular pitching velocity, and the unit vector $\hat{\mathbf{k}}$ is the segment normal direction (Fig. 2a). It is important to mention that the velocity \mathbf{U}_i refers to the component in the plane of the wing segment (spanned by $\hat{\mathbf{k}} - \hat{\mathbf{i}}$; Fig. 2a).

The geometric angle of attack of each blade element can then be calculated from the orientation and velocity of the element with respect to the animal's body in \mathbf{B} , combined with the orientation and velocity of the animal in \mathbf{G} .

Afterward, an induced velocity field is imposed in \mathbf{G} to fully yield the effective angle of attack for each segment [10,11,22,24]. A detailed description of the iterative methods to obtain the induced velocity is adapted from the helicopter literature [50] and was expanded by Parslew [51] to account for an additional induced velocity component parallel to stroke plane. Briefly re-introduced here for completeness, this wake model assumes the stroke plane to be perpendicular to body longitudinal axis. At each time instant, the induced velocity is solved as a function of the aerodynamic forces of the two wings in the frame of the stroke plane. In turn, this induced velocity alters the effective angle of attack that each segment sees, and the two wings would then predict a new value for aerodynamic forces. This iterative wake model is robust and converges quickly—around five iterations for each time step [51]. Similar to a fixed wing of finite wing length, the induced velocity field reduces the angle of attack as evident in Fig. 6, where the cases with wake model (dashed lines) all fall short of those without (solid lines) for both hand (gold)

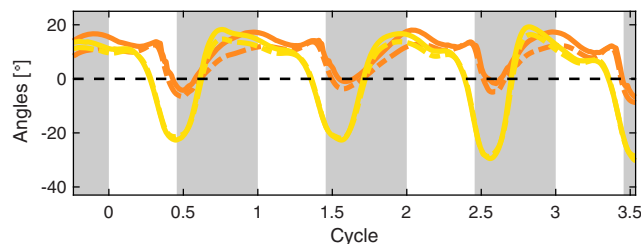


Fig. 6 Effective angle of attack for hand (gold) and arm (orange) wing for the case with wake model (dashed), and no wake model (solid). The gray shades indicate downstroke.

and arm (orange) wings. The effect is more prominent for the arm wing during the downstroke (as much as 10 deg). During the upstroke, the induced velocity is small and has minimal effect on the angle of attack. Note that the fast pronation of the hand wing (large pitching in Fig. 3b) recovers the effective angle of attack from negative to positive around the beginning of the downstroke.

E. Wing Inertia

Bats, unlike insects and many birds, have relatively heavy wings due to the distribution of heavy bones and muscle within the wing structure. *Cynopterus brachyotis* contains around 21% of its total body mass in the wings [12], and it is well-established that the motion of the heavy wings affects the overall body dynamics during both steady and maneuvering flight [12,38,52]. Heavy wings are also a ubiquitous feature of midsized flapping robots. The accelerations associated with flapping and folding of the wings during flight require considerable force, and this must be incorporated into the dynamical model so that the total wing-body interaction is accurately captured.

Figure 7 shows the motion of the wing center of mass (WCoM) in \mathbf{B} . The x , y , and z location of WCoM, $[x_w, y_w, z_w]^T$, is the weighted average over all the wing mass distribution (primarily the bones [12]). The facts that the bones contribute to most of the wing mass and that the proximal bones (humerus, forearm, wrist bones, as well as femur, tibia, and foot; Fig. 7b) are larger and heavier than distal ones (phalanges, or digits) mean that the WCoM should remain close to the body. Over the duration of the wingbeat cycle, the WCoM forms a tight and stable elliptical trajectory in \mathbf{B} (Fig. 7b). Even though the bat is seen to climb slightly in \mathbf{G} , the WCoM trajectory stays unchanged, which hints that the bat achieves this control using finer, localized tuning in the light-weighted wing extremities, rather than the heavy bones near the body.

The distribution of the wing mass also defines wing moments of inertia. Concretely, in the body-fixed frame \mathbf{B} , we define the I_{ij} ($i, j = 1, 2, 3$ for x, y, z) component of the inertia dyadic as

$$I_{ij} \stackrel{\text{def}}{=} \sum_{k=1}^{N_k} m_k (\|\mathbf{r}_k\|^2 \delta_{ij} - x_i^{(k)} x_j^{(k)}) \quad (8)$$

where $k = 1, \dots, N_k$ identifies each bone and $\mathbf{r}_k = (x_1^{(k)}, x_2^{(k)}, x_3^{(k)})$ is the distance of k th bone mass to the WCoM $[x_w, y_w, z_w]^T$, and δ_{ij} is the Kronecker delta. Subsequently, the symmetric and positive definite tensor I_{ij} can be expressed in principal axes and values as $\mathbf{I} = \mathbf{Q} \mathbf{\Lambda} \mathbf{Q}^T$. Here the diagonal matrix $\mathbf{\Lambda}$ represents the principal moment of inertia, I_{xx} , I_{yy} , and I_{zz} , and the principal axes, \mathbf{Q} , can be further decomposed by a set of consecutive Euler angles (Yaw (ψ_w)–Roll (ϕ_w)–Pitch (θ_w)) as $\mathbf{Q} = \mathbf{R}(\theta_w) \mathbf{R}(\phi_w) \mathbf{R}(\psi_w)$. $\mathbf{R}(\cdot)$ here is the rotational matrix.

In Fig. 8a, I_{xx} , which is relevant for the flapping motion, is the largest, followed by I_{zz} , which is associated with a fore-aft sweeping motion; finally I_{yy} , the smallest, resists the pitch rotation along the span. Toward the end of upstroke, I_{zz} approaches I_{xx} in magnitude, which is a direct result of wing protraction (Fig. 8b). Note that, for the case of a rigid wing, the directions of the three principal axes vary in \mathbf{B} , but the magnitude of each component stays the same. Because of the articulation of the wing, however, the magnitudes of the three principal axes ($|I_{xx}|$, $|I_{yy}|$, and $|I_{zz}|$) for the bat wing will also change (Fig. 8b).

For the full-body simulation, the center of mass as well as the moment of inertia are assembled into a left and a right “effective mass” (with an associated moment of inertia) to represent the degrees of freedom for the left and right wings, \mathbf{q}_{lw} and \mathbf{q}_{rw} . For example, for the left wing, $\mathbf{q}_{lw} = [x_{lw}, y_{lw}, z_{lw}, \psi_{lw}, \phi_{lw}, \theta_{lw}]^T$.

F. Lagrangian Equation of Motion

To model the overall motion of the animal, we write the LEoM of the three-point-mass system (two wings and one body) in the global coordinate system \mathbf{G} :

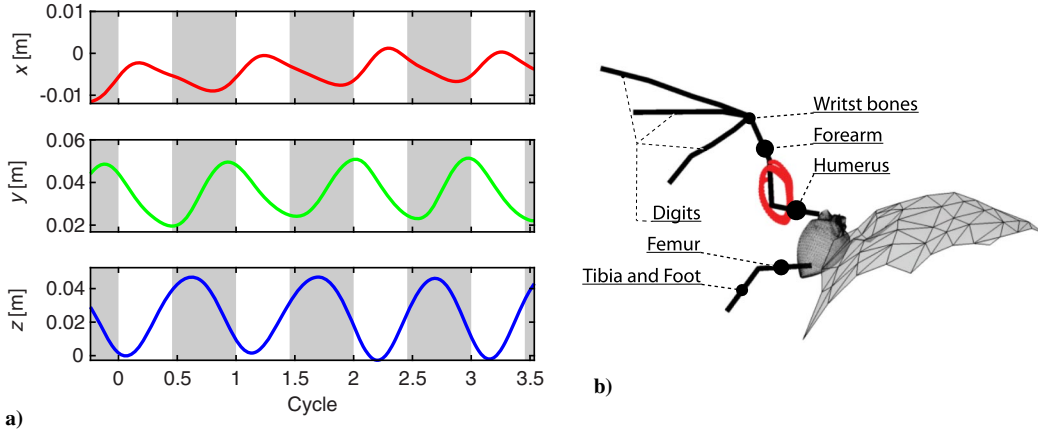


Fig. 7 Wing center of mass (WCoM). a) The x , y , and z location of WCoM is tracked in the body-fixed coordinate B . b) 3D view of WCoM trajectories (red). The relative weights of bones are indicated by size of the filled black circles [12].

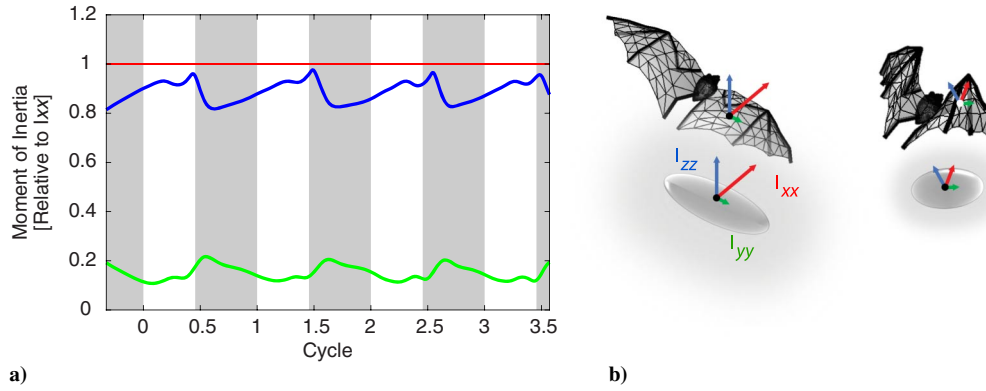


Fig. 8 Principal moment of inertia of the bat wing in body-fixed coordinate B . a) Relative magnitude of the second largest I_{zz} (blue) and smallest I_{yy} (green) normalized by I_{xx} (red). b) The effect of moment of inertia resembles that of an expanding and shrinking ellipsoid.

$$\mathbf{D}(\mathbf{q})\ddot{\mathbf{q}} + \mathbf{C}(\mathbf{q}, \dot{\mathbf{q}})\dot{\mathbf{q}} + \mathbf{g}(\mathbf{q}) = \boldsymbol{\tau} + \mathbf{f}_{\text{aero}} \quad (9)$$

where the generalized coordinate \mathbf{q} has 18 components (6 DoF for the body, and two 6 DoF for each wing). \mathbf{D} , \mathbf{C} , and \mathbf{g} are the mass matrix, centrifugal matrix, and gravitational vector, respectively.

In the right-hand side of Eq. (9), the generalized torque $\boldsymbol{\tau} = [\mathbf{0}_{1 \times 6}, \boldsymbol{\tau}_{\text{lw,int}}, \boldsymbol{\tau}_{\text{rw,int}}]^T$ denotes the internal forces ($\boldsymbol{\tau}_{\text{lw,int}}$, $\boldsymbol{\tau}_{\text{rw,int}}$) between the left/right wing and the body, and the generalized constraint force $\mathbf{f}_{\text{aero}} = [\mathbf{f}_{\text{ext}}, \mathbf{f}_{\text{lw,int}}, \mathbf{f}_{\text{rw,int}}]^T$ represents the aerodynamic forces by the two wings acting on the system (\mathbf{f}_{ext}), and the internal torques, due to aerodynamic forces, on the left and right wing, respectively ($\mathbf{f}_{\text{lw,int}}$, $\mathbf{f}_{\text{rw,int}}$).

Here, because the generalized coordinate \mathbf{q} , its derivatives ($\dot{\mathbf{q}}$, $\ddot{\mathbf{q}}$), and the matrices (\mathbf{D} , \mathbf{C} , and \mathbf{g}) are known from the experimentally measured kinematics, we can directly solve for the x , y , and z components of \mathbf{f}_{ext} , which is essentially the aerodynamic forces required for the animal to follow the observed flight path. This aerodynamic modeling result is obtained purely from the analysis of LEOm, and it is independent of and different from the aforementioned aerodynamic modeling technique, BEMT.

To further test the validity of the aerodynamic model BEMT, we derived the body kinematics using BEMT, and compared this simulated kinematics with experimental recorded data. To this end, at each time t_k , we recognize that the body DoF are related to the first six rows of Eq. (9), and can be rewritten as

$$\mathbf{D}(\mathbf{q})\ddot{\mathbf{q}} = \mathbf{f}_{\text{ext,BEMT}} - (\mathbf{C}(\mathbf{q}, \dot{\mathbf{q}})\dot{\mathbf{q}} + \mathbf{g}(\mathbf{q})) \quad (10)$$

where the known quantities now are \mathbf{q} , $\dot{\mathbf{q}}$ as well as all the system matrices, $\mathbf{D}(\mathbf{q})$, $\mathbf{C}(\mathbf{q}, \dot{\mathbf{q}})$, and $\mathbf{g}(\mathbf{q})$, and unlike previous case, $\ddot{\mathbf{q}}$ at time

step t_k is unknown. The external aerodynamic force $\mathbf{f}_{\text{ext,BEMT}}$ is modeled using BEMT.

Thus, Eq. (10) becomes a linear system (in the form of $\mathbf{A}\mathbf{x} = \mathbf{b}$) at each time t_k , which we solve for the acceleration of the generalized coordinate $\ddot{\mathbf{q}}$. Then, we integrate $\ddot{\mathbf{q}}$ to obtain \mathbf{q} , $\dot{\mathbf{q}}$ at the next time t_{k+1} . In this way, the problem becomes an initial value problem, where the initial conditions at t_0 are provided by the measured state of the animal at the start of the recorded kinematics.

G. Error Estimation: Monte Carlo Simulations

The predictions are sensitive to numerous potential errors, primarily associated with uncertainties in the measured marker location due to stereo triangulation error, in the wind tunnel speed, as well as modeling errors in the constants A , B , and C used in the aerodynamic model [Eq. (5)]. We quantify the effects of this uncertainty by means of Monte Carlo simulations. For each marker position, a sampling with a mean and a standard deviation of 0.05 cm [42] was taken. Similarly the wind tunnel mean flow was assumed to have an uncertainty of ± 0.2 m/s [42]; the modeling constants A , B , and C were assigned a standard deviation of 2%. We ran the simulation 20 times, using kinematics and operating conditions sampled from within these uncertainties, and generated average and standard deviations (error bar) for each computed quantity reported.

III. Results and Discussion

A. Arm and Hand Wing Aerodynamics

The hand and arm wings produce distinctive aerodynamic signatures (Fig. 9). The forces are nondimensionalized by the weight of the animal. The hand wing produces most of the positive thrust during throughout cycle, whereas both arm and hand wing contribute to lift.

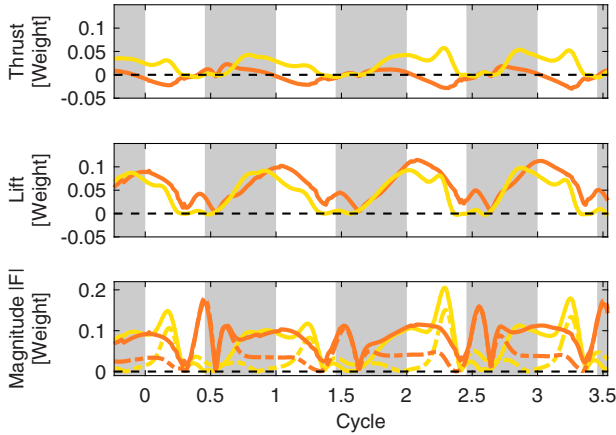


Fig. 9 Aerodynamics of hand (gold) and arm (orange) wings in body-fixed frame **B**. Rotational lift magnitudes (dash lines) are compared with the total force magnitudes (solid lines). The gray shades represent the downstroke.

It also becomes clear that the rotational component of the aerodynamic force, due to the rapid pitching of hand wing during the upstroke (Fig. 3b), creates local thrust peaks in the middle of upstroke, and that the rotation of the arm wing contributes to positive lift even during the upstroke. Similar trend has also been observed by Song et al. [21] in their study of a hovering hummingbird using a blade element analysis. This also agrees with results from PIV measurements by Hubel et al. [15], where they studied the same bat species (*Cynopterus brachyotis*) and found that a vortex pair associated with the arm wing contributes to positive lift. Hedenström et al. [14] arrived at a similar conclusion from measurements obtained with a different bat species, *Glossophaga soricina*. Furthermore, the fact that hand and arm wing have distinctive roles in lift/thrust generation might suggest a need to model them separately, as opposed to lump into one part [22,53].

B. Comparison of Aerodynamic Forces

The predictions of the two distinctive and independent methods used to model the flight mechanics—BEMT and LEOm—are compared in Fig. 10; the cycle-averaged values of lift and thrust are presented in Table 1 in **G**, where the sideslip force F_y is left out as the fluctuation is small due to the left–right symmetric condition in **B** imposed. The average thrust/drag should be zero for a self-propelled

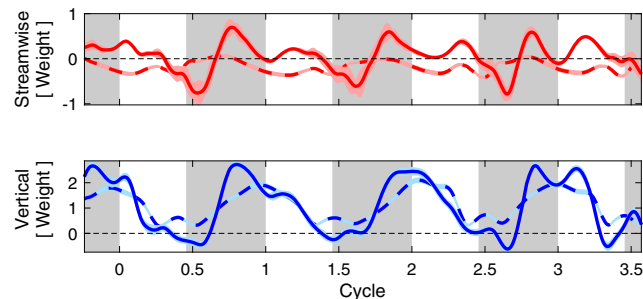


Fig. 10 Aerodynamics forces from two approaches: the BEMT (dashed) and the LEOm (solid). The error bar reflects the impact of uncertainties in the experiment. The gray shades represent the downstroke.

Table 1 Cycle-averaged forces [weight]		
Predicted force	Lagrangian equation of motion	Blade element moment theory
F_x	0.05	−0.16
F_z	1.11	1.10

free flight, and although BEMT underpredicts the average thrust compared with LEOm, both are very small in magnitude and the peaks and troughs align remarkably well. Considering that the BEMT assumes a quasi-steady aerodynamic model that only implicitly accounted for some aspect of a stabilized LEV [7,45], with no knowledge on the unsteady behavior of LEV such as its formation and shedding [23], this level of agreement is quite satisfactory.

For the lift force, both average and instantaneous values predicted by the two schemes match very well and indicate weight support ($F_z \sim 1$ [Weight]), even corroborating the fact that the bat is climbing gently during this trial. The role of rotational lift clearly kicks in near the stroke reversal, when a local peak appears in Fig. 10 at around cycle = 1.5 and 2.5 for both LEOm and BEMT. In addition, both models predict either a small negative (LEOm) or even positive lift (BEMT) during upstroke, which align with a recent CFD study of an insectivorous bat during straight flight [13].

C. Effect of Camber on Aerodynamics

Although low-order models presented by other groups have treated the wing as a flat plate at an angle of attack, we have incorporated wing camber into our modeling—a feature that is particularly important for the compliant membrane wings that are unique to bat flight. An interesting question is how the cambered wing affects the subsequent aerodynamics. Here, we compare the current results with a case where the camber mode in the thin airfoil Fourier series (mode 2 in Fig. 4) is omitted. As seen in Fig. 11, the lift falls when the camber is prominent (late downstroke and early upstroke) as a result of smaller C_L coefficients. The thrust at the same time increases mainly due to the induced lift having a smaller negative projection in the thrust direction, as well as the reduction of C_D . Overall, the cambered wing increases the cycle-averaged lift about 0.27 of the unit weight, but acts to decrease the thrust by 0.1 of the unit weight. Indeed, Gopalakrishnan and Tafti [31], through CFD simulation, reveals that the LEV tends to “glide” over the cambered wing and stays longer in the upper surface than it would for rigid wings, which boosts both lift and thrust generation. Though BEMT assumes a quasi-steady state, the models for C_l and C_d are able to capture some of the stabilized LEV effects that provide the boost in lift generation [7,23,45]. The cycle averaged values are $[F_x, F_z] = [-0.07, 0.84]$ for the no camber simulation, and $[-0.16, 1.10]$ for the case where camber is included.

Note that for a cambered airfoil, according to the classic thin-airfoil theory, the third mode (or “reflex”) from Fourier series relates to the steady moment about quarter-chord (aerodynamic center) location [47]. Typically, this moment coefficients $C_{m,c/4}$ is small (on the order of hundredths) [50] and would induce a small nose-down pitching to the airfoil. However, this effect is not considered in this paper, as very few studies (if any) have measured this moment in a revolving or reciprocating cambered wing to offer empirical data of $C_{m,c/4}$, unlike the empirical values used for C_l and C_d [7,21,40,45,46].

D. Simulated and Observed Body Trajectories

As mentioned earlier, to simulate the evolution of body trajectories, the observed wing kinematics in **B** is used as input, and drive the body forward in global coordinate **G**. Specifically, the acceleration of

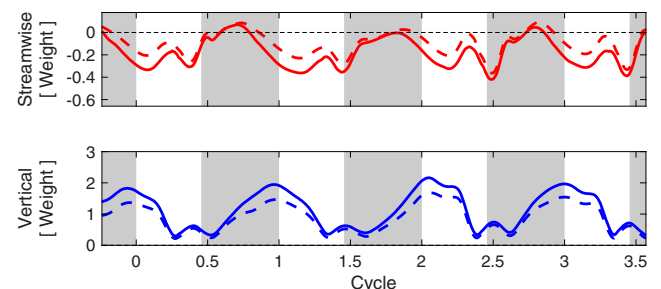


Fig. 11 The aerodynamic effect of camber. The forces generated by the native kinematics (solid) are compared with a hypothetical camber-free case (dashed). The gray shades represent the downstroke.

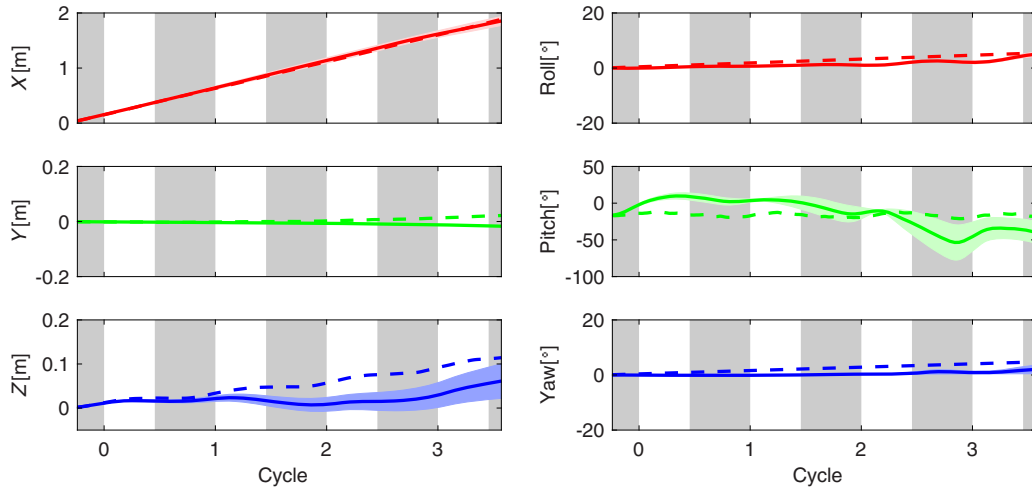


Fig. 12 Comparison of observed (dashed line) and simulated (solid line) body kinematics for 6 DoF in G. The gray shades represent the downstroke.

body position and orientation are solved and integrated over time. This approach improves on the method reported by Windes et al. [13] in that not only the aerodynamics but also the wing inertia is considered, and that not only body position but also orientation is computed and compared with observed trajectories. As seen in Fig. 12, the comparison between the simulated and observed trajectories is very good in X , Y , roll, and yaw (though roll and yaw in this particular flight are both quite small). Particularly, compared with the approach where wing mass is ignored [13], the current method demonstrates better agreement in the streamwise direction X . The simulation does slightly underpredict the vertical (Z) motion, although it is successful in capturing the overall climbing trend. The simulated pitch motion of the body is seen to oscillate around the observed kinematics. Nevertheless, the overall agreement is very encouraging, given the fact that the simulation only uses the left-wing kinematics, whereas the true experiment was not perfectly left-right symmetric.

E. Impact of Body Pitch Moment of Inertia

The body pitch variation and the climbing trend in the vertical direction are strongly tied together, as seen in Fig. 13, where the means of three sets of Monte Carlo simulation results with varying body pitch moment of inertia $I_{yy,body}$ are provided. If we relax the rotational inertia to be half of the original value provided by Riskin et al. [12], the predicted pitch has the worst agreement with that of the observed, and as a result, a descending trend is predicted. On the other hand, if we increase the resistance of the body pitch to be three times its true value, the resulting pitch trend follows closely with that of the observed trend, only to diverge slightly after one complete cycle,

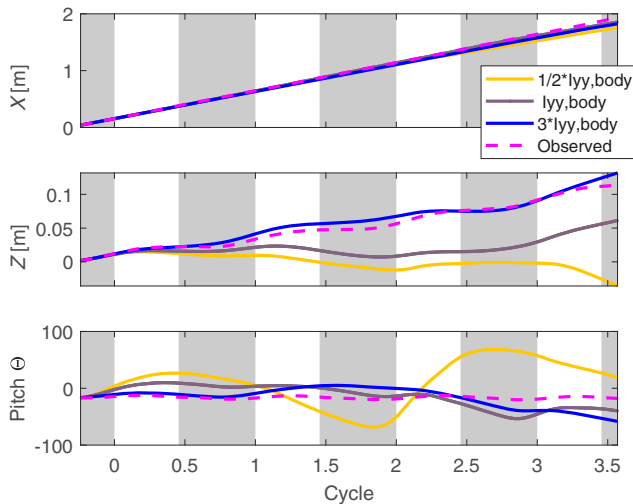


Fig. 13 Sensitivity study on the body pitch moment of inertia $I_{yy,body}$.

potentially due to an accumulated unsteadiness not captured by BEMT. As a result, the climbing trend matches better than the base $I_{yy,body}$ case. It is noted that in all three cases, the reduced $I_{yy,body}$ case predicted the worst agreement along the streamwise X direction, although the sensitivity of X toward change in $I_{yy,body}$ is much more dull. This particular sensitivity on pitch moment of inertia aligns with the most unstable mode found in insect studies as well [54].

IV. Conclusions

A low-order model capable of both modeling and simulating the flight of complex flapping wing systems has been successfully developed, in which the wings are highly articulated, and exhibit variable camber as well as large inertia. The approach has been demonstrated and validated using the previously published data of a bat during flight. It is also noted that the wing kinematics and flexibility come purely from the measured experiment data. Moreover, this approach is applicable to both biological flight as well as human-made robotic flight vehicles. At this time, all of the components of the analysis tool have been successfully implemented, including the calculation of aerodynamic and inertial forces/torques associated with the flapping of heavy wings, as well as the resultant, unconstrained motion of the animal's body in reaction to those forces/torques. Although such low-order models are not completely novel, and BEMT has been in use for decades, the innovative features of the current work include the ability to model the extreme articulation common in bats, which have thin lifting surfaces with variable camber, or aerial robots with compliant membrane wings. The current model provides a completely unconstrained flight simulation, without any symmetry assumptions. The main unsteady aerodynamic effects considered in this paper are the rotational lift [45,46] and the wake model [51], and a future work down the path is to have an explicit formulation for the effect of a stabilized LEV [23]. Although this paper focused on a straight (and relative level) flight trajectories, it is possible that unsteady flow behavior becomes critical for maneuvering or other unsteady flight conditions. On the other hand, although CFD studies undoubtedly resolve detailed unsteady flow behavior in 3D, they too come with assumptions in the scheme, and sometimes special treatment in the kinematics, as discussed in [17], thus might be interpreted with care. The model runs quickly on a laptop or desktop computer and does not have any excessive CPU or memory requirements.

Comparisons between the predictions of BEMT and the LEOm show good agreement in the estimation of thrust/drag, and excellent agreement in the prediction of lift. In another independent validation process, the native wing kinematics was employed to predict aerodynamics using BEMT, and the body would move according to the prediction from LEOm. This simulated body trajectories, in reaction to the recorded wing kinematics, demonstrate good agreement with those observed in the live animal experiments.

In addition to providing trajectory simulations, the model will be able to provide critical insight into the forces, torques, and power required for flight (by muscle or motor). This paper focuses on the description and validation of the method, in order to maintain focus, and it has been applied to an experimental dataset recorded at a single flight speed. However, an important direction will be to apply this model to recorded kinematics recorded at several flight speeds, and to use these to study how the changes in kinematics affect the aerodynamic, inertial forces and the power requirement for flight. This expanded study is currently underway. Having validated the model, one could also use it to study flapping flight with arbitrary kinematics based on other experimental data, robotic vehicles, or idealized theoretical flapping flight model.

Although this approach uses prescribed kinematics to simulate aerodynamic and inertial forces and flight trajectories, a further advancement could use a defined wing geometry and *stiffness*, and prescribe joint torques, generated by muscle or engineered actuators. With this, one could then explore the full fluid–structure interaction. However, this would require an iterative or coupled computation of aerodynamic and elastic/structural forces, and it is well beyond the scope of the current work. Lastly, with further development and in collaboration with more experimental measurements, the model can be used to provide control derivatives and insight into the requirements for the maintenance of stable flight trajectories of both animals as well as flapping flight robots.

Acknowledgments

This work was supported by a grant from the Hyundai Motor Group. Xiaozhou Fan was partially supported by a fellowship from the China Scholarship Council. We are very grateful to Sharon Swartz and the members of the bat flight laboratory at Brown University for many fruitful discussions.

References

- [1] Shyy, W., Aono, H., Kang, C.-K., and Liu, H., *An Introduction to Flapping Wing Aerodynamics*, Cambridge Univ. Press, Cambridge, MA, 2013.
<https://doi.org/10.1017/cbo9781139583916>
- [2] Cheng, B., “Flying of Insects,” *Bioinspired Structures and Design*, Cambridge Univ. Press, United Kingdom, 2020, pp. 271–299.
<https://doi.org/10.1017/9781139058995.012>
- [3] Mountcastle, A. M., and Combes, S. A., “Wing Flexibility Enhances Load-Lifting Capacity in Bumblebees,” *Proceedings of the Royal Society B: Biological Sciences*, Vol. 280, No. 1759, 2013, Paper 20130531.
<https://doi.org/10.1098/rspb.2013.0531>
- [4] Young, J., Walker, S. M., Bomphrey, R. J., Taylor, G. K., and Thomas, A. L. R., “Details of Insect Wing Design and Deformation Enhance Aerodynamic Function and Flight Efficiency,” *Science*, Vol. 325, No. 5947, 2009, pp. 1549–1552.
<https://doi.org/10.1126/science.1175928>
- [5] Nakata, T., and Liu, H., “A Fluid-Structure Interaction Model of Insect Flight with Flexible Wings,” *Journal of Computational Physics*, Vol. 231, No. 4, 2012, pp. 1822–1847.
<https://doi.org/10.1016/j.jcp.2011.11.005>
- [6] Zheng, L., Hedrick, T. L., and Mittal, R., “Time-Varying Wing-Twist Improves Aerodynamic Efficiency of Forward Flight in Butterflies,” *PLoS ONE*, Vol. 8, No. 1, 2013, pp. 1–10.
<https://doi.org/10.1371/journal.pone.0053060>
- [7] Dickinson, M. H., “Wing Rotation and the Aerodynamic Basis of Insect Flight,” *Science*, Vol. 284, No. 5422, 1999, pp. 1954–1960.
<https://doi.org/10.1126/science.284.5422.1954>
- [8] Spedding, G. R., Rosén, M., and Hedenström, A., “A Family of Vortex Wakes Generated by a Thrush Nightingale in Free Flight in a Wind Tunnel over its Entire Natural Range of Flight Speeds,” *Journal of Experimental Biology*, Vol. 206, No. 14, 2003, pp. 2313–2344.
<https://doi.org/10.1242/jeb.00423>
- [9] Pennycuik, J., *Modelling the Flying Bird*, Academic Press, New York, 2008.
<https://doi.org/10.1007/s13398-014-0173-7.2>
- [10] Parslew, B., and Crowther, W. J., “Simulating Avian Wingbeat Kinematics,” *Journal of Biomechanics*, Vol. 43, No. 16, 2010, pp. 3191–3198.
<https://doi.org/10.1016/j.jbiomech.2010.07.024>
- [11] Parslew, B., “Predicting Power-Optimal Kinematics of Avian Wings,” *Journal of the Royal Society Interface*, Vol. 12, No. 102, 2015, Paper 20140953.
<https://doi.org/10.1098/rsif.2014.0953>
- [12] Riskin, D. K., Bergou, A., Breuer, K. S., and Swartz, S. M., “Upstroke Wing Flexion and the Inertial Cost of Bat Flight,” *Proceedings of the Royal Society B: Biological Sciences*, Vol. 279, No. 1740, 2012, pp. 2945–2950.
<https://doi.org/10.1098/rspb.2012.0346>
- [13] Windes, P., Fan, X., Bender, M., Tafti, D. K., Müller, R., and Gurka, R., “A Computational Investigation of Lift Generation and Power Expenditure of Pratt’s Roundleaf Bat (*Hipposideros pratti*) in Forward Flight,” *PLoS ONE*, Vol. 13, No. 11, 2018, Paper e0207613.
<https://doi.org/10.1371/journal.pone.0207613>
- [14] Hedenström, A., Johansson, L. C., Wolf, M., Von Busse, R., Winter, Y., Spedding, G. R., Hedenström, A., Johansson, L. C., Wolf, M., Von Busse, R., Winter, Y., and Spedding, G. R., “Bat Flight Generates Complex Aerodynamic Tracks,” *Science*, Vol. 316, No. 5826, 2007, pp. 894–897.
<https://doi.org/10.1126/science.1142281>
- [15] Hubel, T. Y., Riskin, D. K., Swartz, S. M., and Breuer, K. S., “Wake Structure and Wing Kinematics: The Flight of the Lesser Dog-Faced Fruit Bat, *Cynopterus Brachyotis*,” *Journal of Experimental Biology*, Vol. 213, No. 20, 2010, pp. 3427–3440.
<https://doi.org/10.1242/jeb.043257>
- [16] Hubel, T. Y., Hristov, N. I., Swartz, S. M., and Breuer, K. S., “Wake Structure and Kinematics in Two Insectivorous Bats,” *Philosophical Transactions of the Royal Society B: Biological Sciences*, Vol. 371, No. 1704, 2016, Paper 20150385.
<https://doi.org/10.1098/rstb.2015.0385>
- [17] Viswanath, K., Nagendra, K., Cotter, J., Frauenthal, M., and Tafti, D. K., “Straight-Line Climbing Flight Aerodynamics of a Fruit Bat,” *Physics of Fluids*, Vol. 26, No. 2, 2014, p. 604.
<https://doi.org/10.1063/1.4864297>
- [18] Wang, S., Zhang, X., He, G., and Liu, T., “Numerical Simulation of Unsteady Flows over a Slow-Flying Bat,” *Theoretical and Applied Mechanics Letters*, Vol. 5, No. 1, 2015, pp. 5–8.
<https://doi.org/10.1016/j.taml.2015.01.006>
- [19] Fan, X., Windes, P., Tafti, D., Sekhar, S., Bender, M., Kurdila, A., and Müller, R., “Proper Orthogonal Decomposition of Straight and Level Flight Kinematics in an Insectivorous Bat,” *AIAA Modeling and Simulation Technologies Conference*, AIAA Paper 2018-2155, 2018, p. 1.
<https://doi.org/10.2514/6.2018-2155>
- [20] Ellington, C. P., “The Aerodynamics of Hovering Insect Flight. I. The Quasi-Steady Analysis,” *Philosophical Transactions of the Royal Society of London. B, Biological Sciences*, Vol. 305, No. 1122, 1984, pp. 1–15.
<https://doi.org/10.1098/rstb.1984.0049>
- [21] Song, J., Luo, H., and Hedrick, T. L., “Performance of a Quasi-Steady Model for Hovering Hummingbirds,” *Theoretical and Applied Mechanics Letters*, Vol. 5, No. 1, 2015, pp. 50–53.
<https://doi.org/10.1016/j.taml.2014.12.003>
- [22] Veldani, H. R., Boerma, D. B., Swartz, S. M., and Breuer, K. S., “The Dynamics of Hovering Flight in Hummingbirds, Insects and Bats with Implications for Aerial Robotics,” *Bioinspiration and Biomimetics*, Vol. 14, No. 1, 2019, Paper 016003.
<https://doi.org/10.1088/1748-3190/aac56>
- [23] Taha, H. E., Hajj, M. R., and Beran, P. S., “State-Space Representation of the Unsteady Aerodynamics of Flapping Flight,” *Aerospace Science and Technology*, Vol. 34, No. 1, 2014, pp. 1–11.
<https://doi.org/10.1016/j.ast.2014.01.011>
- [24] Glauert, H., *The Elements of Aerofoil and Airscrew Theory*, Cambridge Univ. Press, Cambridge, MA, 1983, Chaps. 15, 16, <https://www.cambridge.org/core/product/identifier/9780511574481/type/book>.
<https://doi.org/10.1017/cbo9780511574481>
- [25] Osborne, M. F., “Aerodynamics of Flapping Flight with Application to Insects,” *Journal of Experimental Biology*, Vol. 28, No. 2, 1951, pp. 221–245.
<https://doi.org/10.1242/jeb.28.2.221>
- [26] Hedrick, T. L., Usherwood, J. R., and Biewener, A. A., “Low Speed Maneuvering Flight of the Rose-Breasted Cockatoo (*Eolophus roseicapillus*). II. Inertial and Aerodynamic Reorientation,” *Journal of Experimental Biology*, Vol. 210, No. 11, 2007, pp. 1912–1924.
<https://doi.org/10.1242/jeb.002063>
- [27] Clawson, T. S., Fuller, S. B., Wood, R. J., and Ferrari, S., “A Blade Element Approach to Modeling Aerodynamic Flight of an Insect-Scale Robot,” *American Control Conference (ACC)*, 2017, Inst. of Electrical and Electronics Engineers, New York, 2017, pp. 2843–2849.

- [28] Pennycuik, C. J., "Power Requirements for Horizontal Flight in the Pigeon *Columba Livia*," *Journal of Experimental Biology*, Vol. 49, No. 3, 1968, pp. 527–555.
- [29] Sekhar, S., Windes, P., Fan, X., Tafti, D. K., and Borazjani, I., "Canonical Description of Wing Kinematics and Dynamics for a Straight Flying Insectivorous Bat (*Hipposideros pratti*)," *PLoS ONE*, Vol. 14, No. 6, 2019, Paper e0218672.
<https://doi.org/10.1371/journal.pone.0218672>.
- [30] Kang, C. K., Cranford, J., Sridhar, M. K., Kodali, D., Landrum, D. B., and Slegers, N., "Experimental Characterization of a Butterfly in Climbing Flight," *AIAA Journal*, Vol. 56, No. 1, 2018, pp. 15–24.
<https://doi.org/10.2514/1.J055360>
- [31] Gopalakrishnan, P., and Tafti, D. K., "Effect of Wing Flexibility on Lift and Thrust Production in Flapping Flight," *AIAA Journal*, Vol. 48, No. 5, 2010, pp. 865–877.
<https://doi.org/10.2514/1.39957>
- [32] Kang, C. K., and Shyy, W., "Analytical Model for Instantaneous Lift and Shape Deformation of an Insect-Scale Flapping Wing in Hover," *Journal of the Royal Society Interface*, Vol. 11, No. 101, 2014, Paper 20140933.
<https://doi.org/10.1098/rsif.2014.0933>
- [33] Taha, H. E., Woolsey, C. A., and Hajj, M. R., "Geometric Control Approach to Longitudinal Stability of Flapping Flight," *Journal of Guidance, Control, and Dynamics*, Vol. 39, No. 2, 2016, pp. 214–226.
<https://doi.org/10.2514/1.G001280>
- [34] Thollessen, M., and Norberg, U. M., "Moments of Inertia of Bat Wings and Body," *Journal of Experimental Biology*, Vol. 158, No. 1, 1991, pp. 19–35.
<https://doi.org/10.1242/jeb.158.1.19>
- [35] Whitney, J. P., and Wood, R. J., "Aeromechanics of Passive Rotation in Flapping Flight," *Journal of Fluid Mechanics*, Vol. 660, July 2010, pp. 197–220.
<https://doi.org/10.1017/S002211201000265X>
- [36] Cheng, B., and Deng, X., "Translational and Rotational Damping of Flapping Flight and its Dynamics and Stability at Hovering," *IEEE Transactions on Robotics*, Vol. 27, No. 5, 2011, pp. 849–864.
<https://doi.org/10.1109/TRO.2011.2156170>
- [37] Tu, Z., Fei, F., Zhang, J., and Deng, X., "An At-Scale Tailless Flapping-Wing Hummingbird and Experimental Validation," *IEEE Transactions on Robotics*, Vol. 36, No. 5, 2020, pp. 1511–1525.
<https://doi.org/10.1109/TRO.2020.2993217>
- [38] Orlowski, C. T., and Girard, A. R., "Modeling and Simulation of Non-linear Dynamics of Flapping Wing Micro Air Vehicles," *AIAA Journal*, Vol. 49, No. 5, 2011, pp. 969–981.
<https://doi.org/10.2514/1.J050649>
- [39] Biswal, S., Mignolet, M., and Rodriguez, A. A., "Modeling and Control of Flapping Wing Micro Aerial Vehicles," *Bioinspiration and Biomimetics*, Vol. 14, No. 2, 2019, Paper 026004.
<https://doi.org/10.1088/1748-3190/aafc3c>
- [40] Usherwood, J. R., "The Aerodynamic Forces and Pressure Distribution of a Revolving Pigeon Wing," *Experiments in Fluids*, Vol. 46, No. 5, 2009, pp. 991–1003.
<https://doi.org/10.1007/s00348-008-0596-z>
- [41] Sane, S. P., "The Aerodynamics of Insect Flight," *Journal of Experimental Biology*, Vol. 206, No. 23, 2003, pp. 4191–4208.
<https://doi.org/10.1242/jeb.00663>
- [42] Riskin, D. K., Willis, D. J., Iriarte-Diaz, J., Hedrick, T. L., Kostandov, M., Chen, J., Laidlaw, D. H., Breuer, K. S., and Swartz, S. M., "Quantifying the Complexity of Bat Wing Kinematics," *Journal of Theoretical Biology*, Vol. 254, No. 3, 2008, pp. 604–615.
<https://doi.org/10.1016/j.jtbi.2008.06.011>
- [43] Viswanath, K., "Effect of Frontal Gusts and Stroke Deviation in Forward Flapping Flight and Deconstructing the Aerodynamics of a Fruit Bat," Ph.D. Thesis, Dept. of Mechanical Engineering, Virginia Polytechnic Inst. and State Univ., Blacksburg, VA, 2013, p. 144.
- [44] Folch-Fortuny, A., Arteaga, F., and Ferrer, A., "Missing Data Imputation Toolbox for MATLAB," *Chemometrics and Intelligent Laboratory Systems*, Vol. 154, May 2016, pp. 93–100.
<https://doi.org/10.1016/j.chemolab.2016.03.019>
- [45] Wang, Z. J., Birch, J. M., and Dickinson, M. H., "Unsteady Forces and Flows in Low Reynolds Number Hovering Flight: Two-Dimensional Computations vs Robotic Wing Experiments," *Journal of Experimental Biology*, Vol. 207, No. 3, 2004, pp. 449–460.
<https://doi.org/10.1242/jeb.00739>
- [46] Sane, S. P., and Dickinson, M. H., "The Aerodynamic Effects of Wing Rotation and a Revised Quasi-Steady Model of Flapping Flight," *Journal of Experimental Biology*, Vol. 205, No. 8, 2002, pp. 1087–1096.
<https://doi.org/10.1126/science.167.3915.177>
- [47] Anderson, J. D., *Fundamentals of Aerodynamics*, McGraw-Hill Education, New York, 2010, Chap. 4.
- [48] Abbott, I., and von Doenhoff, A., *Theory of Wing Sections*, Vol. 249, Dover, New York, 1950.
[https://doi.org/10.1016/0016-0032\(50\)90516-3](https://doi.org/10.1016/0016-0032(50)90516-3)
- [49] Fung, Y. C., *An Introduction to the Theory of Aeroelasticity*, Dover, New York, 2008.
- [50] Leishman, J. G., *Principles of Helicopter Aerodynamics*, Cambridge Univ. Press, Cambridge, MA, 2006, Chap. 3.
- [51] Parslew, B., "Simulating Avian Wingbeats and Wakes," Ph.D. Thesis, Univ. of Manchester, Manchester, England, U.K., 2012.
- [52] Bergou, A. J., Swartz, S. M., Veldani, H., Riskin, D. K., Reimnitz, L., Taubin, G., Breuer, K. S., and Taylor, G. K., "Falling with Style: Bats Perform Complex Aerial Rotations by Adjusting Wing Inertia," *PLoS Biology*, Vol. 13, No. 11, 2015, Paper e1002297.
<https://doi.org/10.1371/journal.pbio.1002297>
- [53] Ramezani, A., Shi, X., Chung, S. J., and Hutchinson, S., "Lagrangian Modeling and Flight Control of Articulated-Winged Bat Robot," *IEEE International Conference on Intelligent Robots and Systems*, Vol. 2015-Decem, IEEE, New York, 2015, pp. 2867–2874.
<https://doi.org/10.1109/IROS.2015.7353772>
- [54] Sun, M., "Insect Flight Dynamics: Stability and Control," *Reviews of Modern Physics*, Vol. 86, No. 2, 2014, pp. 615–646.
<https://doi.org/10.1103/RevModPhys.86.615>

A. R. Jones
Associate Editor